Shear horizontal wave propagation in a periodic stubbed plate and its application in rainbow trapping

Peng Li [a,b], Li Cheng [a,*]

[a] Department of Mechanical Engineering, The Hong Kong Polytechnic University, Hong Kong, China
[b] School of Human Settlements and Civil Engineering, Xi'an Jiaotong University, Xi'an 710049, PR China

ABSTRACT

The high-order waveguide modal theory, usually used in electromagnetics and acoustics, is adopted to investigate the propagation properties of shear horizontal waves in a periodic stubbed plate. Beyond the sub-wavelength regime, higher-order modes are included to calculate the exact band structures caused by the stubs. Theoretical solutions are obtained in a closed form, in which both the dynamic governing equations and the boundary conditions are strictly satisfied. It is shown that the proposed modelling approach exhibits good convergence and accuracy, in agreement with results obtained from the finite element method. After a systematic investigation on the influence of the stub on the evolution of the band structures, the so-called rainbow trapping phenomenon of SH waves is revealed and explored in a graded stubbed plate with monotonously increasing height or width of the stubs, featuring an obvious reduction of the group velocity and blocking of the wave propagation at different locations for SH waves of different frequencies. The proposed model is expected to provide a useful theoretical tool for the physical mechanism exploration, structural design and eventually system optimization to guide various engineering applications of SH waves.

© 2017 Elsevier B.V. All rights reserved.

1. Introduction

As artificially structured composite materials, acoustic metamaterials (AMs) and phononic crystals (PCs) exhibit anomalous physical properties that cannot be found in nature. Typical examples include absolute band gaps (BGs) [1–3], directional BGs for unidirectional transmissions [4], negative refractions for wave focusing [5], zero-angle refraction for wave collimations [6] and so forth. The diverse functionalities of the AMs and PCs are being explored for various applications, such as cloaking [7], phase manipulation [8], sound absorption [9] and active control [10,11]. The ultimate aim is to be able to manipulate wave propagations through structural design. Conventional PCs and AMs usually consist of two-phase or multi-phase components to create an impedance mismatch as a result of the differences in material properties. Alternatively, the impedance mismatch can also be generated through varying the structural shape or other geometric parameters [12–14]. Acoustic black hole (ABH) structures with the structural thickness tailored in a particular form is a typical example, in which bending waves can be controlled artificially [15,16]. Another example is the periodically corrugated structures made

of the same material in one piece [17], which provides a simple and potential substitution for wave devices, since less design parameters are involved. The advent of new manufacturing capabilities such as 3D printing also makes it possible to fabricate structural components with more complex geometries. Such designs also avoid the joints between multi-phase materials, which are not desirable in manufacturing, assembly and applications.

For the control and the manipulation of elastic waves in a geometry-induced inhomogeneous medium, the primary task is to be able to accurately predict the band structures expressed in terms of the frequency spectrums. Mathematically, it can be expressed in a general form as $G(f) = 0$, in which G stands for an explicit or implicit function of the frequency f. From the mechanical viewpoint, the generalized form of $G(f)$ can be deduced by satisfying the dynamic equations and the corresponding Bloch theorem as the necessary boundary conditions between the unit cells in a periodic structure. However, mathematically, the full dynamic equations describing the elastic wave propagation in solids are governed by the displacement vector, in which the inherent mode coupling needs to be considered. This creates a tremendous challenge for the establishment of the theoretical model allowing for analytical solutions. Hence, most investigations on elastic waves in AMs and PCs have been based on numerical simulations and experiments [12,13,18]. Theoretically, the band structures caused by geometry-induced

* Corresponding author.
  E-mail address: li.cheng@polyu.edu.hk (L. Cheng).

mismatched impedance can be calculated via the revised plane-wave-expansion method [16,19,20], in which virtual vacuum layers need to be added in order to satisfy the traction-free surfaces over the structural portion where geometrical changes take place. In so doing, solutions depend on the thickness of the vacuum layers, and the convergence of the solution is sometimes rather poor. Besides, homogenization methods [21,22] can also be used to obtain the band structure through calculating the effective constitutive parameters of the complex materials, which is known as an efficient tool only for long wavelength approximation. Therefore, theoretical or semi-analytical models, capable of accurately describing the elastic wave propagation in AMs and PCs, are highly desirable. This motivates the present contribution.

Inspired by works in electromagnetics and acoustics [23–26], the high-order waveguide modal theory is utilized to establish a theoretical model on the shear horizontal (SH) wave propagation in a periodic stubbed plate. The model allows for an analytical solution, in which the Bloch theorem is included automatically, which provides much convenience for the mathematical derivation. In the proposed model, higher-order modes are included to get the exact band structures caused by the stubs. The proposed model and the solution show fast convergence by using a small number of terms and high accuracy through comparisons with the result from the finite element method (FEM). Numerical analyses reveal the so-called rainbow trapping phenomenon of SH wave in a graded stubbed plate with monotonously increasing height or width of the stubs, featuring an obvious reduction of the group velocity and blocking of wave propagation at different locations for SH waves of different frequencies.

2. The high-order waveguide mode theory

Consider a periodic stubbed plate with two different additional partial stubs on its upper and bottom surfaces. The plate is assumed unbounded in the x_3 direction, and only a cross section of the unit cell from the stubbed plate is shown in Fig. 1. For convenience, the inhomogeneous plate is divided into three homogeneous regions. Region I is the middle flat plate between the two stubs, whose thickness and periodicity are denoted by $2h$ and l, respectively. Regions II and III correspond to the upper and bottom stubs, occupying the region $|x_2| \leqslant 0.5w^{up}$ and $|x_2| \leqslant 0.5w^{down}$ and having a height of d^{up} and d^{down}, respectively. When a SH wave travels in the inhomogeneous plate, its propagation properties are altered by the geometry-induced mismatched impedance, which will be the focus of the analyses.

The dynamic equation governing the SH waves only involves a displacement component in x_3 direction $u_3 = u(x_1, x_2)$ as

Fig. 1. Scheme of a unit cell from a periodic stubbed plate.

$$\mu\left(\frac{\partial^2 u}{\partial x_1^2} + \frac{\partial^2 u}{\partial x_2^2}\right) = \rho\frac{\partial^2 u}{\partial t^2}, \tag{1}$$

in which μ and ρ are, respectively, the shear modulus and mass density, and t is the time. Given an incident harmonic SH plane wave with an angular frequency ω in the plate, the wave field in the middle plate denoted by Region I can be expressed as [23–27]

$$u^{(I)} = \sum_{\gamma=-\infty}^{\infty} \left[A_\gamma \cos\left(k_{1,\gamma}x_1\right) + B_\gamma \sin\left(k_{1,\gamma}x_1\right)\right] \exp\left(ik_{2,\gamma}x_2\right), \tag{2}$$

in which A_γ and B_γ are the coefficients to be determined and the common term, $\exp(i\omega t)$, has been omitted for brevity. Here, the incident wave field is dropped in Eq. (2), since the dispersion relation, instead of forced vibration, is of the primary concern. As a matter of fact, Eq. (2) can be regarded as the diffraction field caused by the stubs, which is analogue to electromagnetics and acoustics. The eventual inclusion of the incident wave field in Eq. (2) allows the calculation of the reflection and transition coefficients in photonics and phononics [23–26], in which 0-order waveguide mode is usually applied for the sub-wavelength regime. However, beyond the sub-wavelength regime, sufficient higher-order modes should be included in Eq. (2) in order to exactly describe the wave propagation properties of the SH waves. $k_{1,\gamma} = \sqrt{\frac{\omega^2}{c_{SH0}^2} - k_{2,\gamma}^2}$ stands for the wave number in x_1 direction with the bulk velocity $c_{SH0} = \sqrt{\frac{\mu}{\rho}}$. Meanwhile, considering the Bloch theory, the γ-order diffraction wave vector in x_2 direction can be denoted by $k_{2,\gamma} = k + \frac{\gamma \cdot 2\pi}{l}$ with k ranging from $-\pi/l$ to π/l in the irreducible Brillouin zone [27,28]. Based on the solution, the shear stress component can be obtained as

$$T_{31}^{(I)} = \sum_{\gamma=-\infty}^{\infty} \mu k_{1,\gamma}[-A_\gamma \sin\left(k_{1,\gamma}x_1\right) + B_\gamma \cos\left(k_{1,\gamma}x_1\right)] \exp\left(ik_{2,\gamma}x_2\right). \tag{3}$$

The displacement of the SH wave can be expressed by virtue of trigonometric function expansion technique [27,29]. For the upper and bottom stubs, the displacement fields can be written as

$$u^{(II)} = \sum_{n=0,1,2}^{\infty} C_n\left[e^{iq_n^{up}\left(h+d^{up}-x_1\right)} + e^{-iq_n^{up}\left(h+d^{up}-x_1\right)}\right] \cos\left[\alpha_n^{up}(x_2 + 0.5w^{up})\right] \tag{4}$$

$$u^{(III)} = \sum_{m=0,1,2}^{\infty} D_m\left[e^{iq_m^{down}\left(h+d^{down}+x_1\right)} + e^{-iq_m^{down}\left(h+d^{down}+x_1\right)}\right]$$
$$\times \cos\left[\alpha_m^{down}(x_2 + 0.5w^{down})\right], \tag{5}$$

where C_n and D_m are the coefficients to be determined. $\alpha_n^{up} = \frac{n\pi}{w^{up}}$ and $\alpha_m^{down} = \frac{m\pi}{w^{down}}$ are the wave numbers in x_2 direction for the upper and bottom stubs, respectively. Different m and n stand for different modes, symmetrical when $n = m = 0, 2, 4, \ldots$ and anti-symmetrical when $n = m = 1, 3, 5, \ldots$. Actually, the expressions of $u^{(II)}$ and $u^{(III)}$ embrace the principle of the modal superposition method. It should be noted that the traction free boundary conditions $T_{32}^{(II)} = 0$ at $x_2 = \pm 0.5w^{up}$ and $T_{32}^{(III)} = 0$ at $x_2 = \pm 0.5w^{down}$ are automatically satisfied in this case. The wave numbers in the upper and the bottom stubs in x_1 direction can be obtained as $q_n^{up} = \sqrt{\frac{\omega^2}{c_{SH0}^2} - (\alpha_n^{up})^2}$ and $q_m^{down} = \sqrt{\frac{\omega^2}{c_{SH0}^2} - (\alpha_m^{down})^2}$ by ensuring that Eqs. (4) and (5) satisfy the dynamic governing Eq. (1). Correspondingly, the stress components can be obtained as
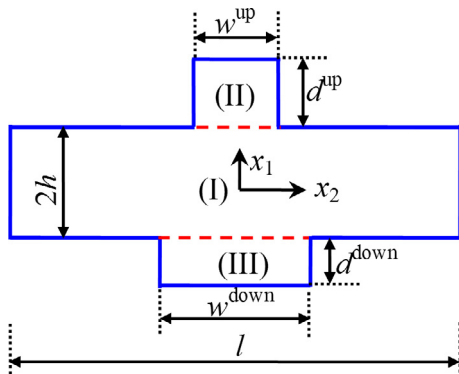
$$T_{31}^{(II)} = \sum_{n=0,1,2}^{\infty} \mu i q_n^{up} C_n \left[-e^{iq_n^{up}(h+d^{up}-x_1)} + e^{-iq_n^{up}(h+d^{up}-x_1)} \right]$$
$$\times \cos\left[\alpha_n^{up}(x_2 + 0.5w^{up})\right], \tag{6}$$

$$T_{31}^{(III)} = \sum_{m=0,1,2}^{\infty} \mu i q_m^{down} D_m \left[e^{iq_m^{down}(h+d^{down}+x_1)} - e^{-iq_m^{down}(h+d^{down}+x_1)} \right]$$
$$\times \cos\left[\alpha_m^{down}(x_2 + 0.5w^{down})\right] \tag{7}$$

Meanwhile, the traction free boundary conditions $T_{31}^{(II)} = 0$ at $x_1 = h + d^{up}$ and $T_{31}^{(III)} = 0$ at $x_1 = -h - d^{down}$ are also automatically satisfied, which provide much convenience for the final solving process. The continuity condition in terms of the displacement and the stress in the regions of $|x_2| \leqslant 0.5w^{up}$ and $|x_2| \leqslant 0.5w^{down}$ at $x_1 = \pm h$ writes

$$x_1 = h : T_{31}^{(I)} = \begin{cases} T_{31}^{(II)}, & |x_2| \leqslant 0.5w^{up} \\ 0, & 0.5w^{up} \leqslant |x_2| \leqslant 0.5l \end{cases} \tag{8a}$$

$$x_1 = h, \ |x_2| \leqslant 0.5w^{up} : u^{(I)} = u^{(II)} \tag{8b}$$

$$x_1 = -h : T_{31}^{(I)} = \begin{cases} T_{31}^{(III)}, & |x_2| \leqslant 0.5w^{down} \\ 0, & 0.5w^{down} \leqslant |x_2| \leqslant 0.5l \end{cases} \tag{9a}$$

$$x_1 = -h, \ |x_2| \leqslant 0.5w^{down} : u^{(I)} = u^{(III)} \tag{9b}$$

Substituting the displacements and the stresses, i.e., Eqs. (2)–(7), into the boundary conditions, i.e., Eqs. (8) and (9), yields

$$\sum_{\gamma=-\infty}^{\infty} k_{1,\gamma} \left[-A_\gamma \sin(k_{1,\gamma}h) + B_\gamma \cos(k_{1,\gamma}h) \right] \exp(ik_{2,\gamma}x_2)$$
$$= \begin{cases} \sum_{n=0,1,2}^{\infty} 2q_n^{up} C_n \sin(q_n^{up}d^{up}) \cos[\alpha_n^{up}(x_2 + 0.5w^{up})], & |x_2| \leqslant 0.5w^{up} \\ 0, & 0.5w^{up} \leqslant |x_2| \leqslant 0.5l \end{cases} \tag{10a}$$

$$\sum_{n=0,1,2}^{\infty} 2C_n \cos(q_n^{up}d^{up}) \cos[\alpha_n^{up}(x_2 + 0.5w^{up})]$$
$$= \sum_{\gamma=-\infty}^{\infty} \left[A_\gamma \cos(k_{1,\gamma}h) + B_\gamma \sin(k_{1,\gamma}h) \right] \exp(ik_{2,\gamma}x_2) \tag{10b}$$

$$\sum_{\gamma=-\infty}^{\infty} k_{1,\gamma} \left[A_\gamma \sin(k_{1,\gamma}h) + B_\gamma \cos(k_{1,\gamma}h) \right] \exp(ik_{2,\gamma}x_2)$$
$$= \begin{cases} \sum_{m=0,1,2}^{\infty} -2q_m^{down} D_m \sin(q_m^{down}d^{down}) \cos[\alpha_m^{down}(x_2 + 0.5w^{down})], \\ \quad |x_2| \leqslant 0.5w^{down} \\ 0, \quad 0.5w^{down} \leqslant |x_2| \leqslant 0.5l \end{cases} \tag{11a}$$

$$\sum_{m=0,1,2}^{\infty} 2D_m \cos(q_m^{down}d^{down}) [\alpha_m^{down}(x_2 + 0.5w^{down})]$$
$$= \sum_{\gamma=-\infty}^{\infty} \left[A_\gamma \cos(k_{1,\gamma}h) - B_\gamma \sin(k_{1,\gamma}h) \right] \exp(ik_{2,\gamma}x_2) \tag{11b}$$

Multiplying Eqs. (10a) and (10b) by $\exp(-ik_{2,\gamma}x_2)$ and $\cos[\alpha_n^{up}(x_2 + 0.5w^{up})]$ respectively, and integrating the individual equation from $-l$ to l and from $-0.5w^{up}$ to $0.5w^{up}$, we can obtain the following linear equations:

$$(\delta_{0n} + 1)w^{up}C_n \cos(q_n^{up}d^{up}) = \sum_{\gamma=-\infty}^{\infty} \left[A_\gamma \cos(k_{1,\gamma}h) + B_\gamma \sin(k_{1,\gamma}h) \right] M_{n\gamma}^{up}, \tag{12a}$$

$$k_{1,\gamma}l[-A_\gamma \sin(k_{1,\gamma}h) + B_\gamma \cos(k_{1,\gamma}h)] = \sum_{n=0,1,2}^{\infty} 2q_n^{up}C_n \sin(q_n^{up}d^{up})\bar{M}_{n\gamma}^{up}, \tag{12b}$$

in which

$$M_{n\gamma}^{up} = \int_{-0.5w^{up}}^{0.5w^{up}} \exp(ik_{2,\gamma}x_2) \cos[\alpha_n^{up}(x_2 + 0.5w^{up})]dx_2$$
$$= \begin{cases} \dfrac{2k_{2,\gamma}\sin(0.5k_{2,\gamma}w^{up})}{k_{2,\gamma}^2 - (\alpha_n^{up})^2}, & n = 0, 2, 4, \ldots \\ \dfrac{2ik_{2,\gamma}\cos(0.5k_{2,\gamma}w^{up})}{k_{2,\gamma}^2 - (\alpha_n^{up})^2}, & n = 1, 3, 5, \ldots \end{cases} \tag{13}$$

in which the bar above the symbols represents the conjugate operation. Applying the similar operation to Eqs. (11a) and (11b) yields

$$(\delta_{0m} + 1)w^{down}D_m \cos(q_m^{down}d^{down})$$
$$= \sum_{\gamma=-\infty}^{\infty} \left[A_\gamma \cos(k_{1,\gamma}h) - B_\gamma \sin(k_{1,\gamma}h) \right] M_{m\gamma}^{down} \tag{14a}$$

$$k_{1,\gamma}l[A_\gamma \sin(k_{1,\gamma}h) + B_\gamma \cos(k_{1,\gamma}h)]$$
$$= \sum_{m=0,1,2}^{\infty} -2q_m^{down}D_m \sin(q_m^{down}d^{down})\bar{M}_{m\gamma}^{down}, \tag{14b}$$

with

$$M_{m\gamma}^{down} = \int_{-0.5w^{down}}^{0.5w^{down}} \exp(ik_{2,\gamma}x_2) \cos[\alpha_m^{down}(x_2 + 0.5w^{down})]dx_2$$
$$= \begin{cases} \dfrac{2k_{2,\gamma}\sin(0.5k_{2,\gamma}w^{down})}{k_{2,\gamma}^2 - (\alpha_m^{down})^2}, & m = 0, 2, 4, \ldots \\ \dfrac{2ik_{2,\gamma}\cos(0.5k_{2,\gamma}w^{down})}{k_{2,\gamma}^2 - (\alpha_m^{down})^2}, & m = 1, 3, 5, \ldots \end{cases} \tag{15}$$

Furthermore, Eqs. (12) and (14) can be simplified as

$$\sum_{\gamma'=-\infty}^{\infty} \left\{ \left[X_{\gamma\gamma'}^{up} \cos(k_{1,\gamma'}h) + k_{1,\gamma}l \sin(k_{1,\gamma}h)\delta_{\gamma\gamma'} \right] A_{\gamma'} \right.$$
$$\left. + \left[X_{\gamma\gamma'}^{up} \sin(k_{1,\gamma'}h) - k_{1,\gamma}l \cos(k_{1,\gamma}h)\delta_{\gamma\gamma'} \right] B_{\gamma'} \right\} = 0, \tag{16a}$$

$$\sum_{\gamma'=-\infty}^{\infty} \left\{ \left[-X_{\gamma\gamma'}^{down} \cos(k_{1,\gamma'}h) - k_{1,\gamma}l \sin(k_{1,\gamma}h)\delta_{\gamma\gamma'} \right] A_{\gamma'} \right.$$
$$\left. + \left[X_{\gamma\gamma'}^{down} \sin(k_{1,\gamma'}h) - k_{1,\gamma}l \cos(k_{1,\gamma}h)\delta_{\gamma\gamma'} \right] B_{\gamma'} \right\} = 0, \tag{16b}$$

where

$$\begin{cases} X_{\gamma\gamma'}^{up} = \sum_{n=0,1,2}^{\infty} q_n^{up} \tan(q_n^{up}d^{up}) \dfrac{2\bar{M}_{n\gamma}^{up}M_{n\gamma'}^{up}}{(\delta_{0n}+1)w^{up}} \\ X_{\gamma\gamma'}^{down} = \sum_{m=0,1,2}^{\infty} q_m^{down} \tan(q_m^{down}d^{down}) \dfrac{2\bar{M}_{m\gamma'}^{down}\bar{M}_{m\gamma}^{down}}{(\delta_{0m}+1)w^{down}} \end{cases} \tag{17}$$

Eqs. (16a) and (16b) contain $2\gamma + 1$ linear algebraic equations with $2\gamma + 1$ undetermined coefficients, containing the frequency $f = \omega/2\pi$. Generally speaking, Eq. (16) contains a set of transcendental equations wherein an explicit expression between the wavenumber k and the frequency f cannot be obtained explicitly. Therefore, a suitable computation method should be developed to solve the problem. For a fixed wavenumber k locating in the region of $[-\pi/l, \pi/l]$, the determinant of the coefficient matrix with

Table 1
Frequencies (kHz) of first several modes in a stubbed aluminum plate with $d = 0.2\ l$ and $w = 0.2\ l$ for different truncations.

$N = 0$	$N = 1$	$N = 2$	$N = 3$	$N = 4$	$N = 5$	$N = 6$
143.69005	133.48111	133.04403	132.91915	132.95037	132.91915	132.85671
N/A	161.54789	160.76739	160.39275	160.14299	160.11177	160.11177
274.18965	236.81931	229.23285	227.60941	227.60941	227.35965	227.04745
N/A	350.89719	326.45193	322.83041	322.73675	322.26845	321.58161
380.83717	353.48845	352.83283	352.55185	352.36453	352.33331	352.33331
461.07257	462.47747	439.81175	437.28293	437.25171	436.90829	436.43999

Table 2
Frequencies (kHz) of first several modes in a stubbed aluminum plate with $d = 0.8l$ and $w = 0.5l$ for different truncations.

$N = 0$	$N = 1$	$N = 2$	$N = 3$	$N = 4$	$N = 5$	$N = 6$
75.322933	64.04783	64.76589	64.45369	64.60979	64.51613	64.57857
87.854641	80.00125	80.03247	79.72027	79.81393	79.72027	79.75149
171.920735	177.68863	175.28469	176.37739	175.94031	176.25251	176.09641
N/A	178.53157	178.68767	178.65645	178.71889	178.71889	178.75011
251.210169	234.91489	235.32075	234.88367	235.07099	234.91489	235.00855
300.977971	305.12867	303.41157	302.78717	302.75595	302.56863	302.59985
N/A	321.83137	321.26941	321.20697	321.20697	321.17575	321.17575
N/A	326.38949	324.89093	324.95337	324.85971	324.89093	324.85971
N/A	355.92361	355.64263	356.11093	356.01727	356.14215	356.11093
372.465527	378.62055	378.68299	378.68299	378.71421	378.71421	378.71421
N/A	409.93421	401.44237	402.22287	401.72335	401.97311	401.78579
N/A	426.44959	416.77139	417.89531	417.11481	417.52067	417.20847
468.192291	452.14365	448.11627	446.39917	446.92991	446.46161	446.71137

A_γ and B_γ as unknowns is evaluated after an initial value of f is introduced. Then, a small increment is added to the frequency until the value of the determinant changes its sign. The "bisection method" is applied finally to locate the root correction.

Focusing on a periodic plate with only one stub on the upper ($d^{up} = 0$ or $w^{up} = 0$) or bottom ($d^{down} = 0$ or $w^{down} = 0$) surface, the dispersion relation can be derived by letting $X_{\gamma\gamma'}^{up}$ or $X_{\gamma\gamma'}^{down}$ in Eq. (16) equal to zero. As a special case, If $d^{up} = d^{down} = 0$ or $w^{up} = w^{down} = 0$, i.e. the plate is flat without stubs, Eq. (16) can be simplified as

$$c = c_{SH0} \sqrt{\left(\frac{m\pi}{2hk_{2,\gamma}}\right)^2 + 1},\ (m = 0, 1, 2, \ldots) \qquad (18)$$

which is the classical phase velocity equation describing the SH wave propagation in a homogeneous plate with its upper and bottom surfaces traction free [30]. When $m = 0$, the phase velocity of the fundamental SH wave, i.e., SH0 wave, is c_{SH0}, which depends on the material properties but is frequency-independent.

3. Numerical simulations

An aluminium plate with a shear modulus $\mu = 26.32$ GPa and a mass density $\rho = 2700$ kg/m^3 is considered [31]. For simplification, the same stubs are attached on the upper and bottom surfaces of the plate, i.e., $w^{up} = w^{down} = w$ and $d^{up} = d^{down} = d$, which means that the stubbed plate is symmetric about x_2-axis, allowing the classification of modes into symmetrical and anti-symmetrical ones. In the simulations, $l = 1$ cm and $2h = 0.5\ l$.

The convergence of the series is firstly examined. Tables 1 and 2 respectively show the frequencies of first several modes in the periodic stubbed plate, solved via Eq. (16), for different truncations of the series when $kl = \pi$. The same truncation order N is used in Eqs. (2), (4) and (5). It can be seen from the tables that the 0-order waveguide mode with $N = 0$ cannot exactly predict the shear horizontal waves in solids, especially for the plate with larger stubs. Therefore, higher order terms need to be included. More

specifically, the solution undergoes relatively fast convergence when N increases in the frequency range of interest. A small number of terms, such as 3, are already sufficient to ensure an acceptable computational accuracy, which will be used in the following simulation. The high-order waveguide modal theory can be viewed as the generalized modal superposition method. Mathematically, the application of the high-order theory is equivalent to the increased number of basis functions, so that the band structure can be accurately described. Physically, it may be understood as an increase in the wave energy transport, carried by the high-order waveguide modes up to a certain order. A suitable truncation order, such as $N = 3$ in the present case, can be applied to guide practical engineering designs of such structures.

The frequency spectrum calculated via Eq. (16) with different stubs is shown in Fig. 2. Meanwhile, results from the Finite Element Method (FEM) with periodic boundary conditions using Comsol Multiphysics software are also given, denoted by circles and triangles for symmetrical and anti-symmetrical modes, respectively. The abscissa with the non-dimensional wave number kl/π, ranging from 0 to 1, represents the first Brillouin zone (the region $[-1, 0]$ is symmetric with that of $[0, 1]$, and has been ignored for simplification). Results of both the symmetrical and anti-symmetrical modes, calculated via Eq. (16), are in good agreement with these from the FEM quantitatively, which validates the established model and the proposed numerical procedure.

Some BGs caused by the stubs emerge, exemplified by five absolute BGs below 500 kHz in Fig. 2(a). Within these bands, the mechanical vibrations in the x_2 direction are suppressed and the propagation of SH waves is prohibited. The corresponding non-dimensional ratio fl/c_{SH0} for the central frequency of the first BG, ranging from 132.6 kHz to 160.2 kHz, is 0.47, suggesting that the formation of the BGs is due to the Bragg scattering effect to some extent. A convex stub, equivalent to an abrupt thickness variation, generates significant impedance mismatch at the joints, which thus creates wave reflections and interferences, and further prohibits the SH wave propagation. When the width of the stub increases to $0.6l$ for a fixed height shown in Fig. 2(b), the first BG is enlarged and the second BG shrinks. On the other hand, if the
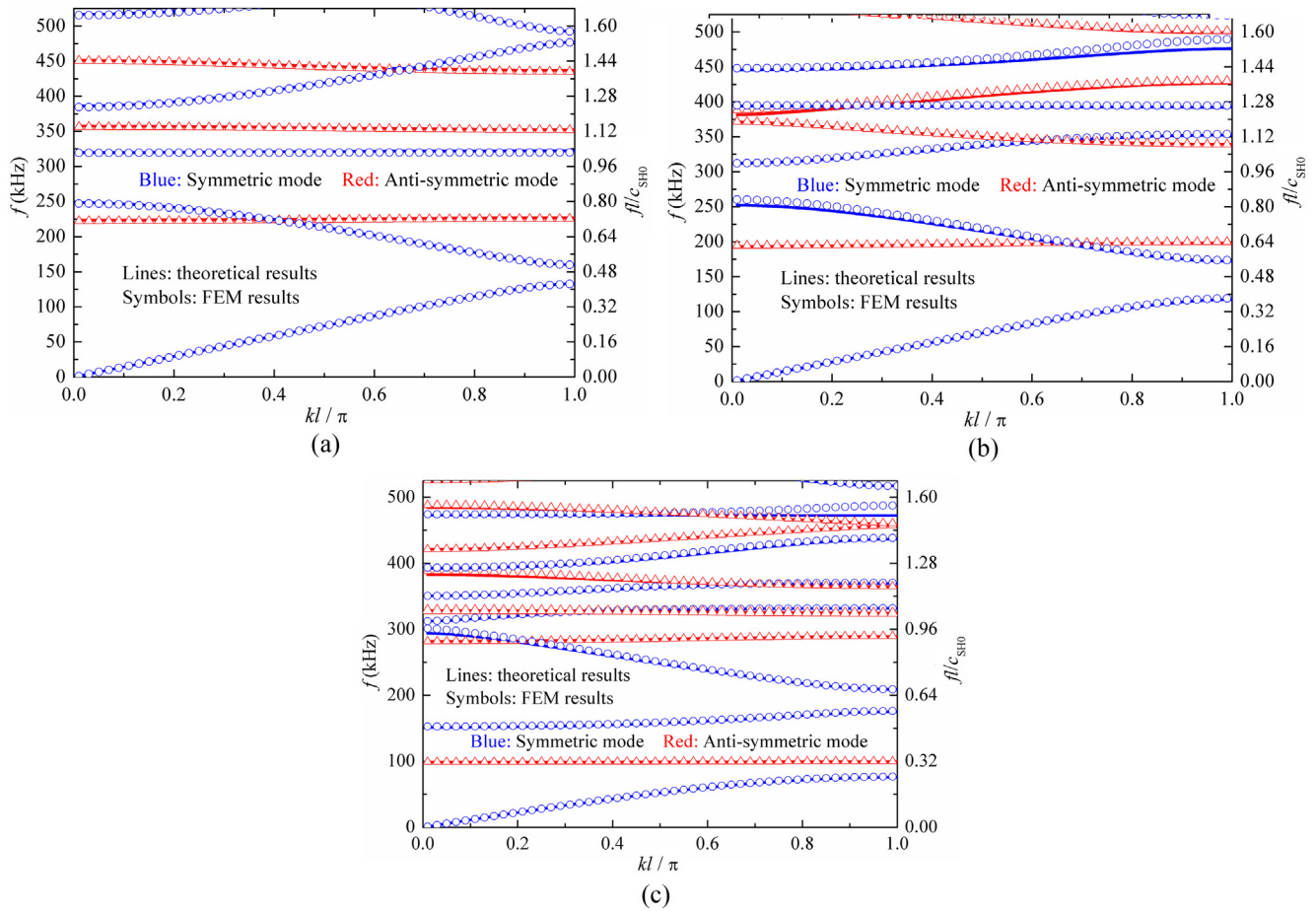
Fig. 2. Frequency spectrum of an infinite periodic stubbed plate: (a) $d = w = 0.2l$; (b) $d = 0.2l$ and $w = 0.5l$; (c) $d = 0.6l$ and $w = 0.5l$. The lines stand for the results calculated using Eq. (16), and symbols with circles and triangles are the results from Comsol Multiphysics software.

height of the stub is further increased for a fixed width, the first BG in Fig. 2(b) is divided into two gaps by the lowest anti-symmetric mode, such as Fig. 2(c). As a general rule, higher modes of the SH waves in an infinite plate have cut-off frequencies which are inversely proportional to the thickness. Therefore, more bands can be seen in Fig. 2(c), compared with Fig. 2(b). As a whole, it can be concluded that the size of the stub, including the height d and the width w, has a great influence on the BGs as well as the SH wave propagation.

In order to better show the effect of the stub on the SH wave propagation characters in the infinite periodic plate, Figs. 3 and 4 respectively show the evolution of the BGs with respect to the height d and the width w of the stub. It can be seen that some new BGs can be opened up and gradually changed with increasing d and w, pointing at the possibility of tuning BGs through changing the height and width of the stub. Almost all the upper and bottom edges of the BGs, except for the upper edge of the first BG, decrease monotonously with the increase of d, attributed to the reduction in the cut-off frequencies of the higher-order modes. For example, the first BG in Fig. 3 originates from the frequency difference between the fundamental SH mode and the first order lateral vibration mode (referred to as 1-order LV mode), with corresponding mode shapes illustrated in Fig. 3. When d increases, the frequency of the 1-order LV mode hardly changes, whilst the frequency of the 1-order SH mode reduces, further cutting the first BG into two parts (red and blue shadows in Fig. 3).

Changing w seems to be more beneficial for the SH wave prohibition, since the width of the BGs in Fig. 4 is larger than that in

Fig. 3. For example, the broadest BG, ranging from 112.7 kHz to 181.5 kHz, can be achieved if w is designed and fixed as $0.67l$. Additionally, the first BG exists between the 0-order and 1-order SH modes, and the corresponding bottom edge first decreases, and then approaches to the lower limit when w is approximately $0.6l$. Owing to the dominance of the lateral vibration as shown in Fig. 4, the lowest frequency of SH wave rebounds again and increases when w further increases.

Generally speaking, the bottom edge of the first BG, i.e., the frequency of the fundamental SH waves, changes continuously when d and w increase. Besides, the corresponding vibration energy is mainly focalized on the stubs, which can be seen from the mode shapes, shown in Figs. 3 and 4. The trapped vibration of the stubs, similar to what is called local resonances, generate wave-slowing phenomenon. Theoretically, the group velocity of the SH waves is reduced, which is evidenced by the relative flat dispersion curve near the edge of the first Brillouin zone, i.e., $kl/\pi = 1$ in Fig. 2. Based on this, an inhomogeneous rainbow trapping structure with graded stubs is proposed in the following part, though which the SH waves can be manipulated artificially and efficiently.

4. Rainbow trapping of the SH waves

An inhomogeneous plate with graded stubs, shown by the shadow region in Fig. 5, is proposed, with the aims of separating SH waves with different frequencies through phase velocity reduction phenomena. Based on the results shown in Figs. 3 and 4 and the
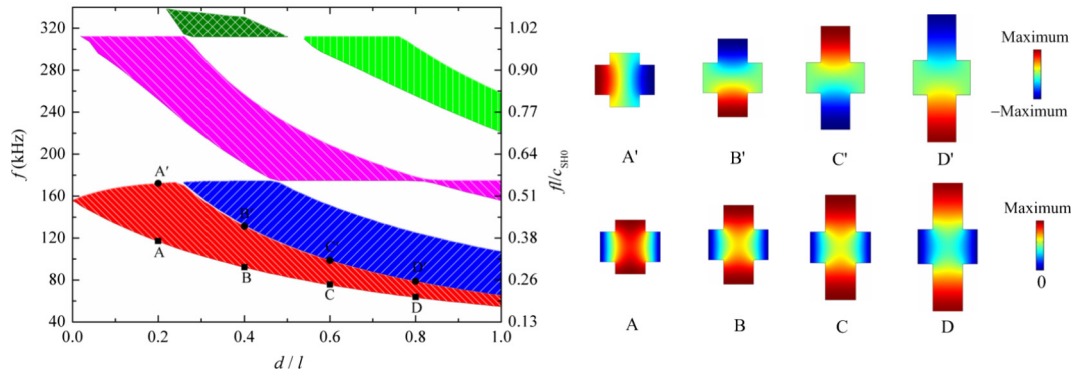
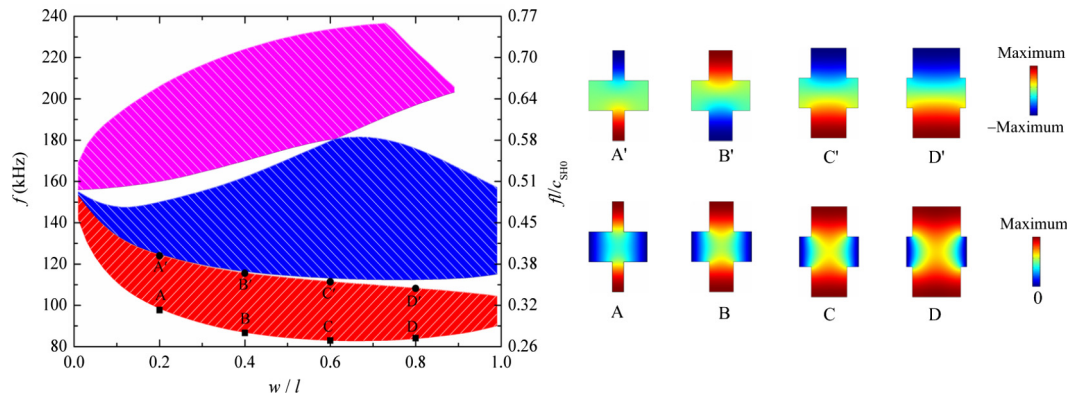**Fig. 3.** Evolution of the BGs with respect to *d* when *w* = 0.5*l*.

Fig. 4. Evolution of the BGs with respect to *w* when *d* = 0.5*l*.
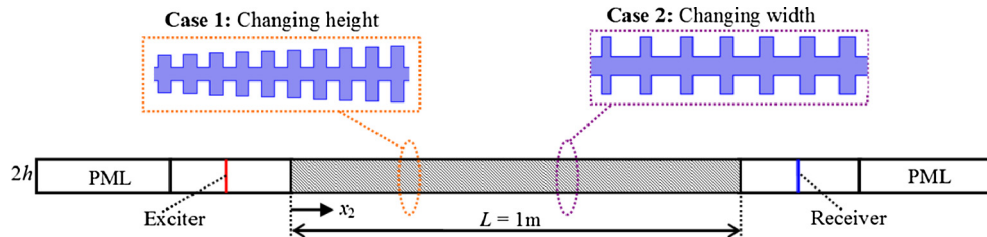

Fig. 5. Schematic of the inhomogeneous plate with graded stubs. 100 pairs of stubs are uniformly distributed on the upper and bottom surfaces of the plate with *d* changing linearly from zero to 0.8*l* in Case 1, and *w* changing linearly from zero to 0.6*l* in Case 2.

discussions above, two types of structural scheme will be designed, each including 100 pairs of stubs distributed on the upper and bottom surfaces of the plate. In Case 1, for the fixed stub width *w*, its height *d* is linearly changed from zero to 0.8*l* in the region $0 \le x_2 \le L$. Case 2 involves the linear width variation from zero to 0.6*l* in the same region, while keeping the height of the stubs constant. Numerical simulations are carried out to show the SH wave trapping phenomena in both frequency and time domains, with the help of the Comsol Multiphysics software.

4.1. Frequency domain analyses

Frequency domain analyses can be viewed as a forced vibration problem. In the simulations, a uniform harmonic shear displacement at different frequencies is applied upstream of the stubbed section of the plate, shown in Fig. 5. Additionally, two perfectly matched layers (PMLs) are adopted over the extended domains at the end of the finite plate in the ±x_2 directions [9–11], to simu-

late the non-reflective infinite boundary conditions. Waves are received at five locations, marked by A, B, C, D and E, with x_2 = 0.2 m, 0.4 m, 0.6 m, 0.8 m and 1.1 m, respectively, with the corresponding of displacement response shown in Fig. 6.

Taking Case 1 for instance (Fig. 6(a)), the response at location E reaches and remains almost zero when the external frequency changes from 64 kHz to 156 kHz, which means the inhomogeneous plate can be used as a wave filter in this frequency range. This is understandable with the help of the band evolution shown in Fig. 3. The first BG changes continuously and monotonously, which means that the linearly distributed neighboring stubs are simultaneously turned on to provide efficient wave blocking. Assuming that the external frequency of the incident SH wave is 120 kHz, the stubs with the height ranging from 0.18*l* to 0.46*l* and distributed from 0.23 m to 0.57 m in Fig. 5, have the ability to prohibit the wave propagating simultaneously, which is enough for the complete wave blocking. For the case E, all of the stubs are available, so that the waves ranging from 64 kHz
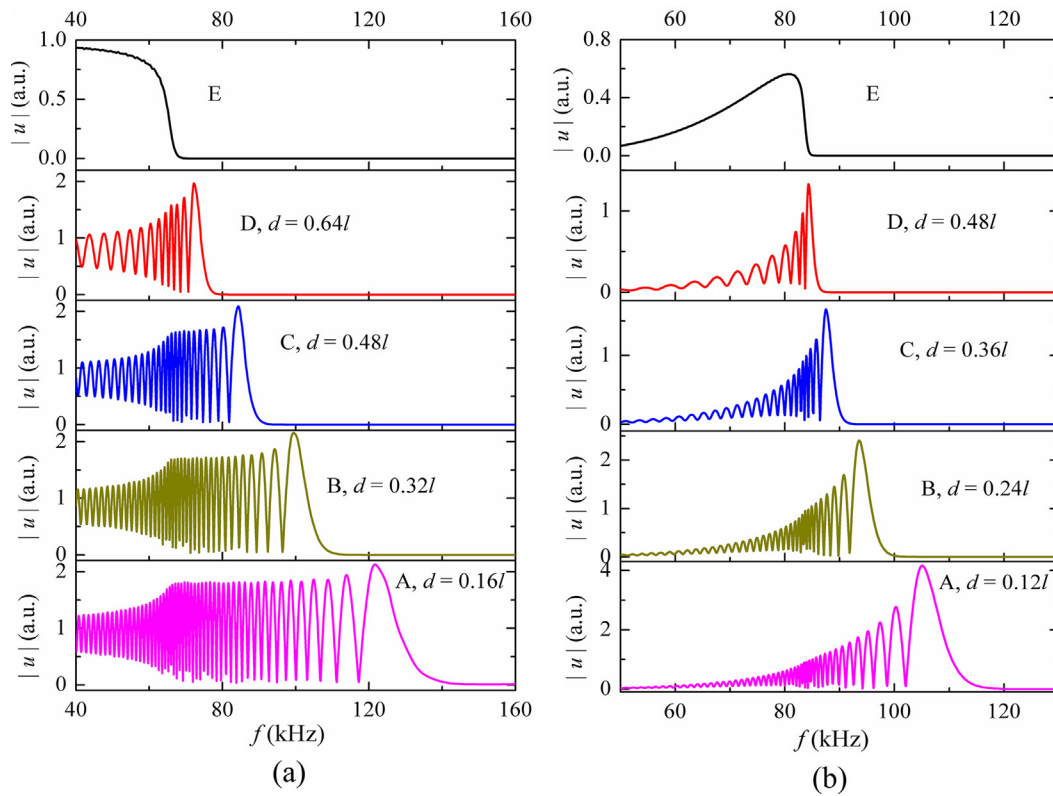
Fig. 6. Amplitude of displacement response versus the incident frequency for: (a) Case 1; (b) Case 2.
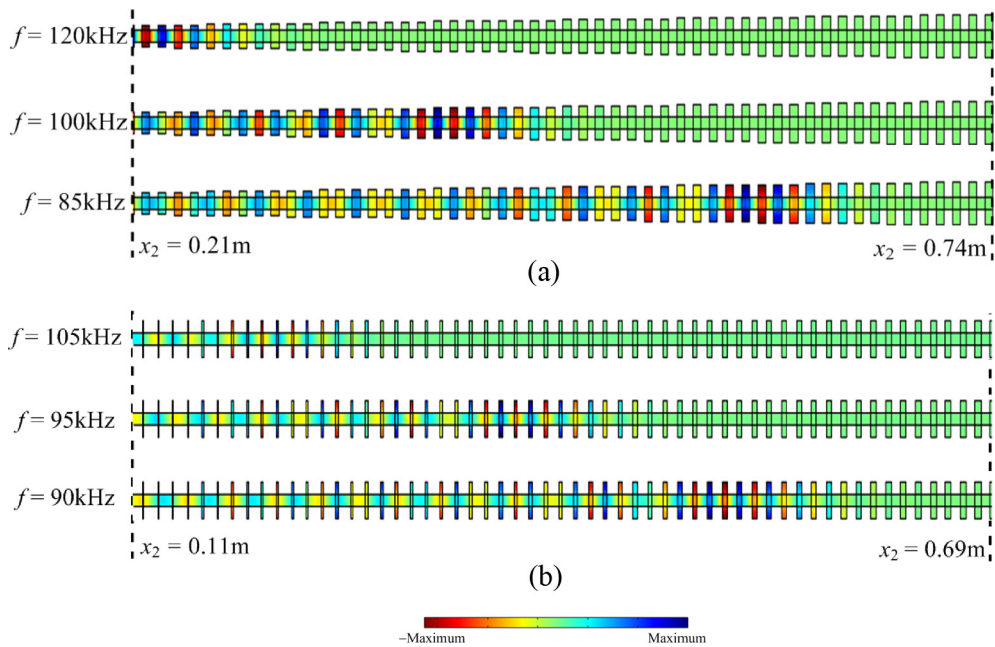

Fig. 7. Displacement distributions of the SH waves at different frequencies for (a) Case 1, and (b) Case 2.

to 156 kHz are prohibited. However, at other receiving positions, such as B, only the stubs within the region $0 \leq x_2 \leq 0.4$ m take effect, generating a low-pass effect only starting from 110 Hz. Note this low-pass behavior takes place at different locations along the structure, lower frequency traveling over longer distance and vice versa. But ultimately, wave stops propagating at a certain location. This phenomenon can be referred to as fre-

quency separation or frequency shunting. The same phenomena can be observed in Case 2, as shown in Fig. 6(b), with the changing width of the stubs. The displacement distribution along the propagation direction for different frequencies is shown in Fig. 7 for a few selected frequencies, which clearly depict this phenomenon. From Fig. 6, we can observe the so-called inner resonance phenomenon, corresponding to the highest peak just
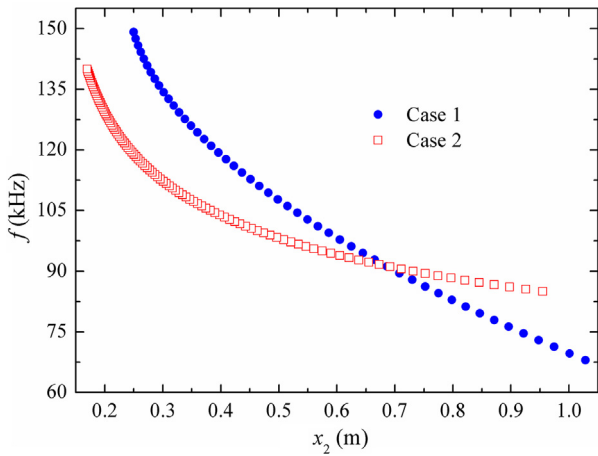
Fig. 8. Relationship between the wave frequency and the stop location defined for the two cases.

before the attenuation region, in agreement with the work by Cao et al. [28] and Hussein et al. [32].

In order to quantify the observed frequency separation or frequency shunting phenomenon, a non-dimensional ratio $\delta(x_2) = |u'(x_2)|/|u|$ is defined, in which $|u|$ is the amplitude of the incident SH waves and $|u'(x_2)|$ stands for the amplitude of the evanescent waves. Furthermore, a critical value, $\delta_c = 0.01$, is adopted to quantify the wave-blocking location, which stands for the longest distance that a SH wave can travel with 99% amplitude attenuation. Smaller than δ_c, the incident SH waves are considered as being stopped. Fig. 8 shows the relationship between the wave frequencies and the stop location for the two cases discussed above. Again, it can be seen that waves with lower frequencies can travel a longer distance. For frequencies larger than about 90 kHz, SH waves in the stubbed plate with graded heights travel a longer distance than their counterparts with graded widths. Due to the wave slowing-down and energy trapping phenomena around the stop locations, sensors or energy harvesters can be designed and artificially arranged at these positions of the plate,
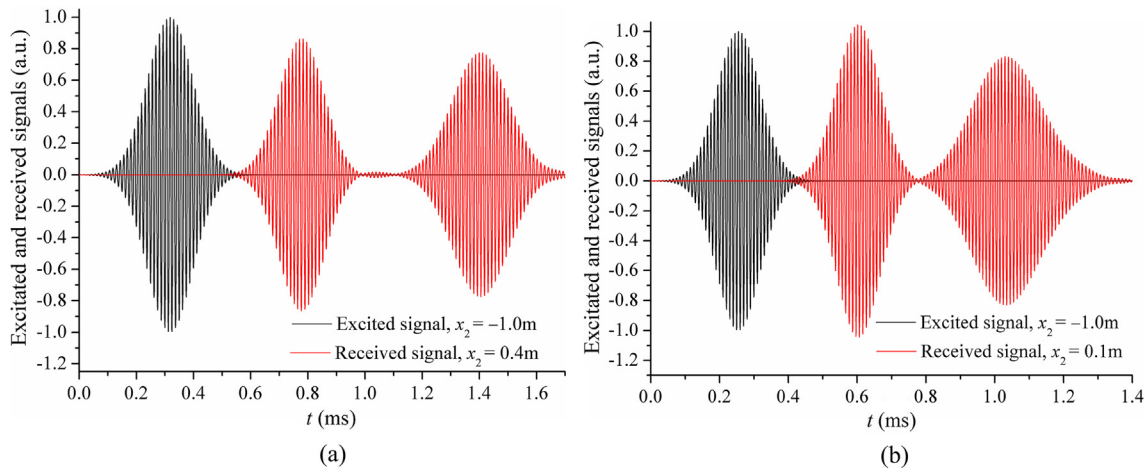

Fig. 9. Some transient horizontal displacement signals for different conditions: (a) Case 1, f_0 = 80 kHz, and x_2 = 0.4 m; (b) Case 2, f_0 = 100 kHz, and x_2 = 0.1 m.
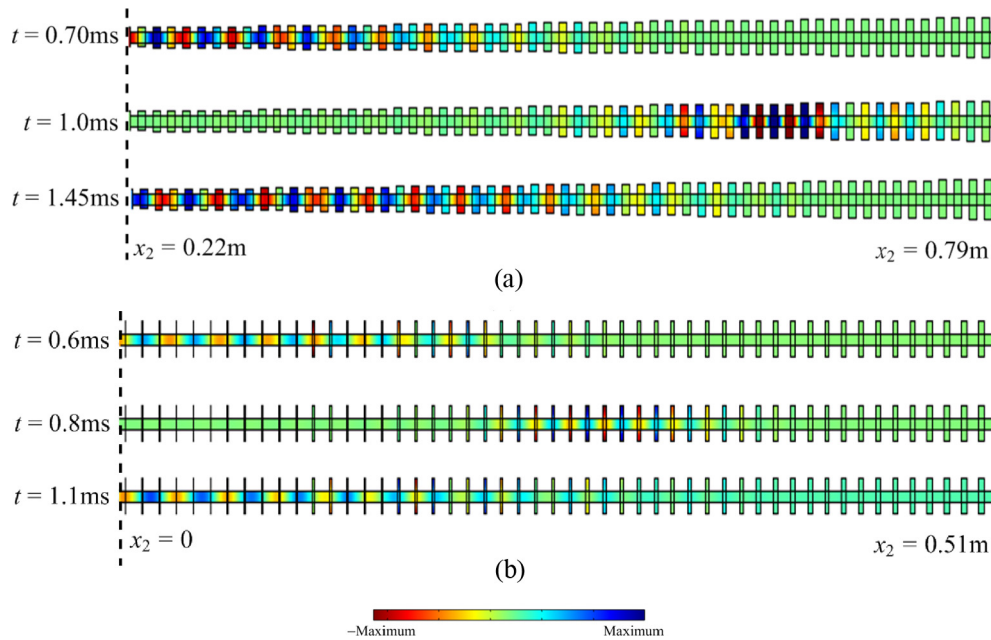

Fig. 10. Displacement profiles of the SH waves at some specific time instants to illustrate the wave incidence and reflection for: (a) Case 1; and (b) Case 2.
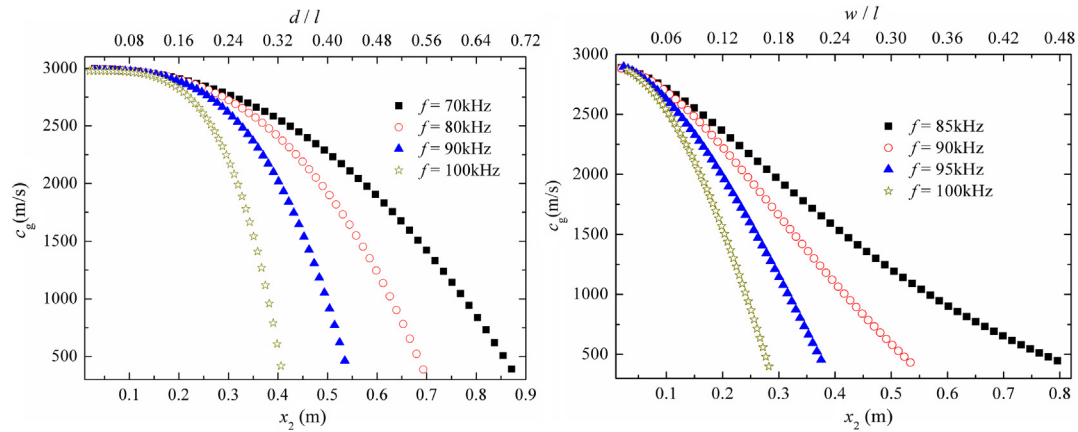
Fig. 11. Calculated group velocities of the SH waves propagating along the inhomogeneous plate with graded stubs for: (a) Case 1; and (b) Case 2.

so that the SH waves with different frequencies can be picked up according to specific requirements.

4.2. Time domain analyses

In order to better show the slowing-down process of the SH wave through the graded stubs, time domain analyses are performed with a transient excitation. A Gaussian pulse with a fixed central frequency f_0, shown by the black lines (the first wave packet) in Fig. 9, is imposed at $x_2 = -1.0$ m. The plate domain used in Fig. 5 is adjusted to eliminate wave reflections caused by the left boundary of the plate within the computation time concerned. In the FEM simulations, the finite mesh sizes in space are set to be smaller than 1/20 of the smallest wavelength under consideration and the time step smaller than $1/20f_0$ [33]. Besides, re-computation is conducted using finer mesh sizes to make sure that the numerical results are convergent and accurate.

Two wave response packets are captured inside the region with graded stubs, shown by the red lines in Fig. 9 within the time window considered. The first response packet is the displacement when an incident SH wave travels along the graded stubbed plate. The maximum amplitude of the response packets is gradually reduced, as compared with the incident excitation wave, which is due to the reflection during the wave propagation. The second response packet corresponds to the reflected signal caused by Bragg scattering effect. The reflection can also be directly seen by the Gaussian signal profiles snapshotted at several time points depicted in Fig. 10. For example, compared with the displacement profiles at $t = 1.0$ ms in Fig. 10(a), the SH waves are reflected and propagate along $-x_2$ direction at $t = 1.45$ ms.

Using the received signal at different positions, the group velocity c_g can be calculated, with results shown in Fig. 11, which clearly shows the slowing-down process of the SH waves for different frequency components. For Case 1, the stubs have little effect on the group velocity when the height is smaller than $0.12l$. When $x_2 > 0.15$ m, c_g decreases evidently. However, for the stubs with graded widths, the group velocity undergoes continuous reduction along x_2 direction. This difference can be explained by considering the mode shapes shown in Figs. 3 and 4. For Mode A shown in Fig. 4, most of the vibration energy is focalized within the stubs, which means that the wave energy inside the plate is taken away by the attached stubs and trapped temporarily when wave arrives, leading to an obvious reduction in the group velocity. On the contrary, for Mode A in Fig. 3, the vibration energy is distributed in the regions of short stubs and the connecting area of the plate. Therefore, the lagging effect on the SH waves is less pronounced when

the height of the stubs is small, so that the group velocity almost keeps unchanged. Additionally, with the reducing velocity, the wavelength becomes shorter and compressed in the propagation process. This leads to a strong energy concentration, which is consistent with the time-domain signals picked up at $t = 1.0$ ms in Fig. 10(a) and $t = 1.45$ ms in Fig. 10(b).

In summary, when a broadband SH wave packet propagates through the graded stubbed plate, wave components with different frequencies are slowed down in different ways, then spatially split, stopped and trapped at different locations, in line with the so-called "rainbow trapping" in electromagnetics and acoustics [34].

5. Conclusions

A theoretical model, which can simultaneously satisfy the governing dynamic equations and the boundary conditions for the SH waves propagation in a periodic stubbed plate, is established in a closed form based on the high-order waveguide modal theory and the trigonometric function expansion technique. The model allows for exact solutions. The convergence of the solutions is demonstrated and the theoretical model is numerically validated with the aid of the FEM results using a stubbed aluminum plate. Systematic investigations are carried out to demonstrate the influence of the stubs on the SH wave propagation, leading to the design of a stubbed plate allowing for the realization of the so-called rainbow trapping phenomenon. Major conclusions are drawn as follows:

(1) The proposed high-order waveguide modal theory has been proved to be effective and accurate for the simulation of the SH wave propagation in an elastic plate with periodic stubs. The approach guaranties fast convergence and computation accuracy by using a small number of series terms.

(2) Bragg BGs are shown to exist. The size of the stub, including the height and width, has a great influence on the formation and the evolution of Bragg BGs. This allows for the SH waves to be manipulated artificially in order to achieve specific wave propagation effects.

(3) The rainbow trapping of the SH waves can be achieved through graded stubs distributed on both surfaces of an elastic plate, in which incident wave components with different frequencies can be slowed down in different manners, spatially split, stopped and trapped at different locations along the propagation path. Due to the wave slowing-down phenomena and energy trapping around the stop

locations, sensors or energy harvesters can be designed and artificially arranged at these positions of the plate, so that the SH waves with different frequencies can be picked up according to specific requirements.

It is relevant to note that, due to its relative simplicity, the proposed theoretical model provides a flexible tool to guide the design of such structures to cater for different engineering applications. Not restricted to elastic media, the theoretical methodology and the dynamic analysis framework presented in this paper can also be extended to the transversely isotropic media straightforwardly, e.g., piezoelectric and magneto-electro-elastic materials and structures. The issue of mechanical-electrical coupling and other complicating factors such as nonlinear elastic waves in phononics deserves a separate and systematic investigation in further work.

Acknowledgment

References

[1] Z.H. Qian, F. Jin, F.M. Li, K. Kishimoto, Complete band gaps in two-dimensional piezoelectric phononic crystals with 1–3 connectivity family, Int. J. Solids Struct. 45 (2008) 4748–4755.
[2] Y.Z. Wang, F.M. Li, W.H. Huang, Y.S. Wang, The propagation and localization of Rayleigh waves in disordered piezoelectric phononic crystals, J. Mech. Phys. Solids 56 (2008) 1578–1590.
[3] Y.Z. Wang, F.M. Li, K. Kishimoto, Y.S. Wang, W.H. Huang, Wave localization in randomly disordered periodic piezoelectric rods with initial stress, Acta Mech. Solida Sin. 21 (2008) 529–535.
[4] B. Yuan, B. Liang, J.C. Tao, X.Y. Zou, J.C. Cheng, Broadband directional acoustic waveguide with high efficiency, Appl. Phys. Lett. 101 (2012) 043503.
[5] J. Bucay, E. Roussel, J.O. Vasseur, P.A. Deymier, A.-C. Hladky-Hennion, Y. Pennec, K. Muralidharan, B. Djafari-Rouhani, B. Dubus, Positive, negative, zero refraction, and beam splitting in a solid/air phononic crystal: theoretical and experimental study, Phys. Rev. B 79 (2009) 214305.
[6] W. Liu, X.Y. Su, Collimation and enhancement of elastic transverse waves in two-dimensional solid phononic crystals, Phys. Lett. A 374 (2010) 2968–2971.
[7] A.N. Norris, A.L. Shuvalov, Elastic cloaking theory, Wave Motion 48 (2011) 525–538.
[8] Y.B. Xie, W.Q. Wang, H.Y. Chen, A. Konneker, B.-I. Popa, S.A. Cummer, Wavefront modulation and subwavelength diffractive acoustics with an acoustic metasurface, Nat. Commun. 5 (2014) 5553.
[9] J. Mei, G.C. Ma, M. Yang, Z.Y. Yang, W.J. Wen, P. Sheng, Dark acoustic metamaterials as super absorbers for low-frequency sound, Nat. Commun. 3 (2012) 756.
[10] Y.Y. Chen, G.L. Huang, Active elastic metamaterials for subwavelength wave propagation control, Acta Mech. Sin. 31 (2015) 349–363.
[11] Y.Z. Wang, F.M. Li, Y.S. Wang, Influences of active control on elastic wave propagation in a weakly nonlinear phononic crystal with a monoatomic lattice chain, Int. J. Mech. Sci. 106 (2016) 357–362.
[12] A.-C. Hladky-Hennion, C. Granger, J. Vasseur, M. Billy, Propagation of elastic waves in one-dimensional periodic stubbed waveguides, Phys. Rev. B 82 (2010) 104307.
[13] A. Climente, D. Torrent, J. Sánchez-Dehesa, Gradient index lenses for flexural waves based on thickness variations, Appl. Phys. Lett. 105 (2014) 064101.
[14] S. Tol, F.L. Degertekin, A. Erturk, Gradient-index phononic crystal lens-based enhancement of elastic wave energy harvesting, Appl. Phys. Lett. 109 (2016) 063902.
[15] L.L. Tang, L. Cheng, H.L. Ji, J.H. Qiu, Characterization of acoustic black hole effect using a one-dimensional fully-coupled and wavelet-decomposed semi-analytical model, J. Sound Vib. 374 (2016) 172–184.
[16] H.F. Zhu, F. Semperlotti, Phononic thin plates with embedded acoustic black holes, Phys. Rev. B 91 (2015) 104304.
[17] S. Banerjee, T. Kundu, Elastic wave propagation in sinusoidally corrugated waveguides, J. Acoust. Soc. Am. 119 (2006) 2006–2017.
[18] T.-C. Wu, T.-T. Wu, J.-C. Hsu, Wave guiding and frequency selection of Lamb waves in a plate with a periodic stubbed surface, Phys. Rev. B 79 (2009) 104306.
[19] Z.L. Hou, B.M. Assouar, Modeling of lamb wave propagation in plate with two-dimensional phononic crystal layer coated on uniform substrate using plane-wave-expansion method, Phys. Lett. A 372 (2008) 2091–2097.
[20] J.O. Vasseur, P.A. Deymier, B. Djafari-Rouhani, Y. Pennec, A.-C. Hladky-Hennion, Absolute forbidden bands and waveguiding in two-dimensional phononic crystal plates, Phys. Rev. B 77 (2008) 085415.
[21] W.J. Parnell, T. Shearer, Antiplane elastic wave cloaking using metamaterials, homogenization and hyperelasticity, Wave Motion 50 (2013) 1140–1152.
[22] C. Caloz, A. Lai, T. Itoh, The challenge of homogenization in metamaterials, New J. Phys. 7 (2005) 1–14.
[23] R.A. Jahdali, Y. Wu, High transmission acoustic focusing by impedance-matched acoustic meta-surfaces, Appl. Phys. Lett. 108 (2016) 031902.
[24] F.Y. Cai, F.M. Liu, Z.J. He, Z.Y. Liu, High refractive-index sonic material based on periodic subwavelength structure, Appl. Phys. Lett. 91 (2007) 203515.
[25] F.J. Garcia-Vidal, L. Martin-Moreno, J.B. Pendry, Surfaces with holes in them: new plasmonic metamaterials, J. Opt. A – Pure Appl. Opt. 7 (2005) S97–S101.
[26] P. Peng, B.M. Xiao, Y. Wu, Flat acoustic lens by acoustic grating with curled slits, Phys. Lett. A 378 (2014) 3389–3392.
[27] Y.L. Xu, Analytical study of dispersion relations for shear horizontal wave propagation in plates with periodic stubs, Ultrasonics 61 (2015) 114–120.
[28] W.W. Cao, W.K. Qi, Plane wave propagation in finite 2–2 composites, J. Appl. Phys. 78 (1995) 4627–4632.
[29] B.X. Zhang, A. Bostrom, A.J. Niklasson, Antiplane shear waves from a piezoelectric strip actuator: exact versus effective boundary condition solutions, Smart Mater. Struct. 13 (2004) 161–168.
[30] Y. Liu, V.K. Chillara, C.J. Lissenden, J.L. Rose, Third harmonic shear horizontal and Rayleigh Lamb waves in weakly nonlinear plates, J. Appl. Phys. 114 (2013) 114908.
[31] W.S. Zhou, H. Li, F.G. Yuan, Guided wave generation, sensing and damage detection using in-plane shear piezoelectric wafers, Smart Mater. Struct. 23 (2014) 015014.
[32] M.I. Hussein, G.M. Hulbert, R.A. Scott, Dispersive elastodynamics of 1D banded materials and structures: analysis, J. Sound Vib. 289 (2006) 779–806.
[33] Y.L. Xu, P. Peng, High quality broadband spatial reflections of slow Rayleigh surface acoustic waves modulated by a graded grooved surface, J. Appl. Phys. 117 (2015) 035103.
[34] J. Zhu, Y.Y. Chen, X.F. Zhu, F.J. Garcia-Vidal, X.B. Yin, W.L. Zhang, X. Zhang, Acoustic rainbow trapping, Sci. Rep. 3 (2013) 1728.